

A Novel Full-Polarization SAR Images Ship Detector Based on the Scattering Mechanisms and the Wave Polarization Anisotropy

Chuan Zhang^a, Gui Gao^a, Linlin Zhang^a, C. Chen^b, S. Gao^{c,*}, Libo Yao^d, Qilin Bai^a, Shiquan Gou^a

^aFaculty of Geosciences and Environmental Engineering, Southwest Jiaotong University, Chengdu, China

^bthe National University of Defense Technology, Changsha, China

^cHunan University, Changsha, China

^dNaval Aviation University of China

Abstract

Synthetic aperture radar (SAR) is considered being a good option for earth observation with its unique advantages. In this paper, we proposed an adaptive ship detector using full-polarization SAR images. First, by thoroughly investigating the scattering characteristics between ships and their background, and the wave polarization anisotropy, a novel ship detector is proposed by jointing the two characteristics, named Scattering-Anisotropy joint (joint-SA). Based on the theoretical analysis, we showed that the joint-SA is an effective physical quantity to show the difference between the ship and its background, and thus joint-SA can be used for ship detection of full-polarization image data. Second, the generalized Gamma distribution (GFD) was used to characterize the joint-SA statistics of sea clutter with a large range of homogeneity. As a result, an adaptive constant false alarm rate (CFAR) method was implemented based on the joint-SA. Finally, RADARSAT-2 and GF-3 data in C-band and ALOS data in L-band are used for verification. We tested on five datasets, and the experimental results verify the correctness and superiority of the constant false alarm rate (CFAR) method based on the joint-SA. In addition, the experimental results also showed that the signal-clutter ratio (SCR) of the proposed ship detector joint-SA (33.17 dB, 35.98 dB, 57.25 dB) is better than that of DBSP (8.92 dB, 3.43 dB, 25.40 dB) and RsDVH (17.28 dB, 11.17 dB, 54.55 dB). More importantly, the proposed detector joint-SA has higher detection accuracy and a lower false alarm rate.

Keywords: Synthetic Aperture Radar (SAR), Scattering Mechanism, Wave Polarization Anisotropy, Relatively Weakly Scattering Targets

1. Introduction

With the development of satellite technology, synthetic aperture radar (SAR) plays an increasingly important role in various fields, because of its capability in imaging day and night without considering the weather condition, such as land-cover classification (Ohki and Shimada, 2018), change detection (Ciuonzo et al., 2017), disaster damage estimation (Chini et al., 2017), maritime traffic control (Renga et al., 2018), inversion of surface parameters (Hajnsek et al., 2003) and so on. Particularly, ship detection using SAR images is an effective means of ocean monitoring because the ship's position information can help the government deal with illegal

*Corresponding Author: gaosh8899@126.com

fishing (Snapir et al., 2019), illegal immigration, and so on. However, the detection of ships using SAR images is a complex and important topic, not only because of the sophistication of the ships themselves but also because of the sophistication and variability of the marine environment, especially for small targets, where the detection difficulty rises dramatically.

In the past decades, algorithms of ship detection using SAR images data have been extensively researched, and it has got many credible results. Among the existing models, the constant false alarm rate (CFAR) detector based on the statistical model of the sea clutter is a classical ship detection model and is widely used (Robey et al., 1992; Wackerman et al., 2001). Meanwhile, Gaussian distributions, Weibull (Schleher, 1976), Gamma (Principe et al., 1998), K (Jakeman and Tough, 1987), and Generalized K distribution (Ferrara et al., 2011; Liao et al., 2008) were used to describe the statistical of the sea clutter. The generalized Gamma distribution (Martín-de Nicolás et al., 2014) (GFD) can get higher fitting accuracy than other statistical models and has been experimentally proven to be effective.

In the early stage of using single-polarization SAR image to detect, Y Jeremy et al. (Jeremy et al., 2001) found that, at low incidence angles, the HV polarization has the highest SCR, which is the average value over the number of pixels, and the HH polarization has better SCR at high incidence angles. Tian et al. (Tian et al., 2015) proposed a ship detection method based on target enhancement and non-parametric clutter estimation using single-polarization SAR image, which not only improves the uniform image and non-uniform image of the ship-sea contrast, and adaptively estimated the clutter distribution in the enhanced image. However, single-polarization SAR data cannot provide rich polarization information, so its detection performance will be dramatically reduced in complex sea conditions.

Compared with the single-polarization SAR data, multi-polarization data contains richer information on backscattering and phase and provides a much more comprehensive characterization of the polarization information of complex sea conditions. Based on the dual-polarization SAR data, Gao et al. (Gao et al., 2013) proposed a ship CFAR detection method, which constructs a new PMA detector with improved ship SCR and makes it easier to detect ships from clutter. Shirvany et al. (Shirvany et al., 2012) based on the fact that the degree of polarization (DoP) can describe the fundamental quantity of partially polarized electromagnetic fields, studied the performance of DoP by combining ship and oil-spill detection under different polarization in hybrid, compact, and linear dual-pol SAR images.

Since the full-polarization data can completely reflect the scattering characteristics of the target, more and more researchers are interested in using full-polarization data for ship detection. Traditional ship detection algorithms, such as the total power detector (SPAN), the polarimetric whitening filter (PWF) (Liu et al., 2019), the power-maximization synthesis (PMS) (Chaney et al., 1990) detector, etc. directly fuse the intensity information of the scattering matrix to perform ship detection. Although these detectors can achieve excellent results in the sea state of calm, their detection effectiveness decreases sharply when the sea state is complex. Therefore, by taking full advantage of the rich information from the full-polarization SAR data, a detection method that combines the high-resolution capability of X-band sensors with the removal of azimuthal ambiguity for ship detection has been proposed by Velotto et al. (Velotto et al., 2013).

However, even though these detectors have proved the ability to distinguish ships from sea clutter, the detection performance of intensity or amplitude-based methods is susceptible to sea conditions. Compared to the use of intensity of amplitude or intensity information, an alternative approach is to use polarization decomposition to explore new detectors. Using the similarity parameter (SP) (Yang et al., 2001) of surface scattering, An et al. (AN et al., 2009) added the term “1-SP” into the PMS to form the new detector. Marino et al. (Marino et al., 2012) proposed a geometrical perturbation-polarimetric notch filter (GP-PNF) derived from the complex space of polarized targets to detect targets at sea. Yang et al. (Yang et al., 2019) proposed PolSAR

image saliency detection based on weighted perturbation filters. Zhang et al. (Zhang et al., 2019) proposed a new detection algorithm based on improving the geometrical GP-PNF. Based on non-negative matrix factorization (NMF), Guo et al. (Guo et al., 2011) proposed a new strategy for ship detection. This strategy uses non-negative eigenvalues to estimate sparsity from histograms that can reveal the sparse distribution of eigenvalues. Combining non-negative and sparse features, this method can be flexible and efficient for ship detection. Cloude et al. (Cloude and Pottier, 1996) used polarization parameters, such as entropy and eigenvalues, for ship detection. But it has been studied that these two detectors are not suitable for the detection of small targets in complex scenes. Zhang et al. (Zhang et al., 2017) used full-polarization SAR images to generate the polarimetric covariance difference matrix (CP) to improve the local contrast of the images and then extracted Shannon entropy features from them for the ship detection. The effectiveness of the method has been proved on the GF-3.

Ships and other man-made objects on the surface of the ocean are complex metallic structures with complex scattering mechanisms (SM). Freeman et al. (Freeman and Durden, 1998) proposed a three-component model that decomposes the scattering power of the target as: surface scattering, due to direct backscattering from surfaces perpendicular to the radar beam; double-bounce scattering, because of the dihedral formed by the vertical ship’s conducting plates and the sea surface; volume scattering, formed because of multiple bouncing of electromagnetic waves (Velotto et al., 2013). Based on the three-component model, Yamaguchi et al. (Yamaguchi et al., 2005) proposed a four-component scattering model by adding the helix scattering characteristics. Through combining the double-bounce scattering, volume scattering, and helix scattering from the complete polarimetric covariance difference matrix, Zhang et al. (Zhang et al., 2018) proposed a new detector, named (for simplicity, we call this detector “DBSP” in this paper). Experiments showed that the detection results outperformed the other ship detectors. Based on the DBSP detector, Zhang et al. (Zhang et al., 2020) used the similarity parameter of the surface scattering to construct a new detector named RsDVH. The effectiveness of the detector RsDVH was proved experimentally.

Although the above detectors have experimentally proven their effectiveness, they still lose their effectiveness for some relatively weakly scattering targets, especially in the complex sea condition. More seriously, the robustness of existing detectors is not good, and their detection accuracy is not guaranteed across different types of satellite platforms or different bands of data.

Overall, the existing ship detector can’t effectively detect ships, especially for some relatively weakly scattering targets on the condition of the high sea state. In this paper, by jointing the scattering characteristics of the target and the wave polarization anisotropy, we proposed a new full-polarization SAR image ship detector named joint-SA. Therefore, the contribution of this paper is:

- 1) From two different perspectives, a new ship detector joint-SA is proposed based on the target scattering characteristics and the wave polarization anisotropy. This detector can be seen as a joint of scattering power and wave polarization anisotropy to highlight the difference between the target and its background. From the perspective of SCR and detection accuracy, we also proved that the detector is an effective physical quantity for ship detection.
- 2) We tested and verified the suitability of the for characterizing joint-SA statistics of sea clutter with a wide range of homogeneity. We also implemented adaptive detection of full-polarization SAR images by combining the CFAR algorithm and GFD.
- 3) The correctness of the theoretical analysis and the superiority of the CFAR method based on joint-SA detection were verified by experiments on the GF-3 in C-band, RADARSAT-2 in C-band, and ALOS in L-band.

The remainder of this paper is arranged as follows. Section 2 simply describes the theoretical background. In Section 3, the details of detector joint-SA are stated carefully. Comparison

experiments with different detectors are performed in Section 4. Conclusions and discussion are given in Section 5 .

2. Theoretical Background

In this section, we mainly reviewed the basic theoretical knowledge in SAR image processing, including the scattering matrix [S], covariance matrix [C].

Full-Polarization (FP) SAR can measure the complete backscatter information of the target and comprehensively characterize the scattered power of the target, usually using a scattering matrix (Guissard, 1994) to characterize the information of each element of SAR image, which is defined as(Lee and Pottier, 2017)

$$[S] = \begin{bmatrix} S_{HH} & S_{HV} \\ S_{VH} & S_{VV} \end{bmatrix} \quad (1)$$

where S_{pq} denotes the p-transmitted and q-received scattering element. H indicates horizontal polarization wave, V indicates vertical polarization wave.

In real scenarios, the targets observed by SAR satellites are not ideal scattering mechanisms, but a combination of multiple objects called partial targets (Deschamps and Mast, 1973). The two-dimensional scattering matrix cannot effectively characterize all the properties of the target, so the second-order statistics of the scattering matrix are introduced (Marino, 2013). We assume that the scattering matrix satisfies the reciprocity theorem. When k is expressed in the Pauli basis, i.e., $[k]=[S_{HH}, \sqrt{2}S_{HV}, S_{VV}]$, then the covariance matrix can be expressed as

$$\begin{aligned} [C] &= \langle k \cdot k^T \rangle \\ &= \begin{bmatrix} \langle |S_{HH}|^2 \rangle & \langle \sqrt{2}S_{HH}S_{HV}^* \rangle & \langle S_{HH}S_{VV}^* \rangle \\ \langle \sqrt{2}S_{HV}S_{HH}^* \rangle & \langle 2|S_{HV}|^2 \rangle & \langle \sqrt{2}S_{HV}S_{VV}^* \rangle \\ \langle S_{VV}S_{HH}^* \rangle & \langle \sqrt{2}S_{VV}S_{HV}^* \rangle & \langle |S_{VV}|^2 \rangle \end{bmatrix} \\ &= \begin{bmatrix} C_{11} & C_{12} & C_{13} \\ C_{21}^* & C_{22} & C_{23} \\ C_{31}^* & C_{32}^* & C_{33} \end{bmatrix} \end{aligned} \quad (2)$$

where $\langle \cdot \rangle$ represents ensemble averaging; superscript “*” is the complex conjugate; and $|\cdot|$ denotes the modulus of the complex signal.

3. Scattering-Anisotropy Joint and Adaptive Detection

3.1. Four-component Decomposition

To better characterize the scattering mechanism of the target, Yamaguchi et al.(Yamaguchi et al., 2005) decomposed the scattering mechanism of the target into four components, namely surface scattering P_s , double-bounce scattering P_d , volume scattering P_v , and helix scattering P_h . The decomposition of the equation is given by

$$\begin{aligned} \langle [C] \rangle &= f_s \langle [C] \rangle_s + f_d \langle [C] \rangle_d + f_v \langle [C] \rangle_v + f_h \langle [C] \rangle_h \\ &= f_s \begin{bmatrix} |\beta|^2 & 0 & \beta \\ 0 & 0 & 0 \\ \beta^* & 0 & 1 \end{bmatrix} + f_d \begin{bmatrix} |\alpha|^2 & 0 & \alpha \\ 0 & 0 & 0 \\ \alpha^* & 0 & 1 \end{bmatrix} \\ &\quad + f_v \begin{bmatrix} a & 0 & b \\ 0 & c & 0 \\ d & 0 & e \end{bmatrix} + \frac{f_h}{4} \begin{bmatrix} 1 & \pm j\sqrt{2} & -1 \\ \mp j\sqrt{2} & 2 & \pm j\sqrt{2} \\ -1 & \mp j\sqrt{2} & 1 \end{bmatrix} \end{aligned} \quad (3)$$

where the parameters a, b, c, d, and e are determined by $10\log \frac{\langle |S_{VV}|^2 \rangle}{\langle |S_{HH}|^2 \rangle}$. In addition, the $P_s = f_s(1 + |\beta|^2)$, $P_d = f_d(1 + |\alpha|^2)$, $P_v = f_v$ and $P_h = f_h$; P_s , P_d , P_v , and P_h should satisfy $P_t = P_s + P_d + P_v + P_h = \langle |S_{HH}|^2 + 2|S_{HV}|^2 + |S_{VV}|^2 \rangle$.

Inspired by (Yamaguchi et al., 2005), through utilizing the complete polarimetric covariance difference matrix [CP], Zhang et al. (Zhang et al., 2018) proposed a new detector $DBSP_{CP}$ (for convenience, we will call it “DBSP” in this paper)

$$DBSP_{CP} = ((P_d)_{CP} + (P_v)_{CP}) \cdot (P_h)_{CP} \quad (4)$$

Although the effectiveness of the DBSP detector was proved on several data sets, the detector still has some drawbacks, as stated in (Zhang et al., 2020). First, the algorithm of DBSP removes the surface scattering feature, so the detector loses the ability to detect ships when they primarily exhibit surface scattering. Second, the [CP] is calculated based on the fact that the target pixel differs from its surrounding pixels in terms of the polarized scattering. That is, when the scattering difference between the target pixel and the surrounding pixels is not obvious, the value of the target pixels may be small or even zero, and then DBSP loses its detection effectiveness.

To overcome the disadvantages of the DBSP detector, Zhang et al. (Zhang et al., 2020) proposed a new detector RsDVH

$$RsDVH = Rs_{max} \cdot ((P_d)_{max} + (P_v)_{max}) \cdot (P_h)_{max} \quad (5)$$

where the subscript “max” indicates the selection of the maximum value from the values calculated by [C] and [CP], and Rs_{max} ($0 \leq Rs_{max} \leq 1$) denotes the parameter associated with surface scattering.

Although the RsDVH detector is experimentally proven to be superior to the DBSP detector, our careful analysis of RsDVH reveals that there is a contradiction in equation (5). On the one hand, when the target pixel exhibits mainly surface scattering, that is to say, $Rs_{max} \rightarrow 1$, and the values of $(P_d)_{max}$, $(P_v)_{max}$, and $(P_h)_{max}$ are small. On the contrary, when other scattering mechanisms prevail, the $Rs_{max} \rightarrow 0$, and the values of $(P_d)_{max}$, $(P_v)_{max}$, and $(P_h)_{max}$ are large. In other words, Rs_{max} is inversely related to $((P_d)_{max} + (P_v)_{max}) \cdot (P_h)_{max}$. On the other hand, when Rs_{max} and $((P_d)_{max} + (P_v)_{max}) \cdot (P_h)_{max}$ are multiplied, the two do not serve to highlight the target pixels and suppress clutter pixels. This is the paradox of the detector RsDVH.

3.2. Scattering-Anisotropy Joint

As described in section 3.1, the ship detectors DBSP and RsDVH exist some disadvantages. To improve the detection of the accuracy of relatively weakly scattering targets, we urgently need a new characteristic independent of the target scattering mechanism which is joint with the target scattering characteristics to overcome the shortcomings in the detectors DBSP and RsDVH. Hence, we introduced a new physical quantity—wave polarization anisotropy ΔS . This is for two reasons. First, the article (Zhang et al., 2018, 2020) demonstrated that it is feasible to use the difference in scattering mechanisms between the ship and the clutter for detection. Second, the wave polarization anisotropy can characterize target non-stationary (Touzi et al., 2004), which can compensate for the limitation of the detector DBSP and RsDVH depending only on the scattering characteristics. It should be noted that at incidence angles less than 60° , the values of ΔS for the ocean are generally lower than those for ships, just as the paper (Touzi et al., 2004) stated.

As we all know, ships and other man-made objects at sea exhibit complex scattering mechanisms, and it is the sophistication of the target scattering mechanisms that can be described by

the extreme value of the degree of polarization (DoP). Using the DoP , Bicout et al. (Bicout and Brosseau, 1992) introduced a measure of the wave entropy S , which was given by

$$S(DoP) = -\ln(s(DoP)) \quad (6)$$

where $s(x) = \frac{1}{2}(1+x)^{\frac{1+x}{2}}(1-x)^{\frac{1-x}{2}}$ and $S(DoP)$ is a bijective, strictly decreasing function of DoP , and should satisfy $S(DoP = 1) \leq S \leq S(DoP)$. The normalized value $S_n(DoP) = S(DoP)/S(0)$ takes values between 0 and 1. The variations of scattered wave purity DoP with transmitting wave polarization produce a change of the wave entropy (Touzi et al., 2004).

The $S(DoP)$ is directly related to DoP which is characterizing the purity of the scattered wave. The dynamic range ΔS is directly related to the dynamic range of Δ_{DoP} and thus can provide a measure of the complexity of the scattering mechanism (Touzi et al., 1992). This leads to the expression for the wave polarization anisotropy as given (Touzi, 2000)

$$\Delta S_n = S_n(DoP_{min}) - S_n(DoP_{max}) \quad (7)$$

where the extreme values were derived by the method introduced by the Kostinski et al. (Kostinski et al., 1988). Therefore, we introduced wave polarization anisotropy ΔS_n to characterize the non-stationarity of the target. The larger the value of ΔS_n , the greater the variation of the signal with transmit-receive polarization (Touzi et al., 2004).

As mentioned earlier, the scattering mechanisms alone cannot provide effective detection of relatively weakly scattering targets, such as detectors DBSP and RsDVH. Therefore, we proposed a new full-polarization SAR image ship detector joint-SA; and the expression of the joint-SA is given by

$$joint - SA = (P_d + P_v) \cdot P_h \cdot \Delta S \quad (8)$$

where P_d , P_v , P_h denote double-bounce scattering, volume scattering, and helix scattering, respectively; and ΔS_n represents the wave polarization anisotropy. It should be noted that P_d , P_v , P_h are calculated from $[C]$ and not $[CP]$. There are two advantages to doing this. On the one hand, it can overcome the defects in the DBSP. On the other hand, it avoids complex operations and improves the efficiency of the algorithm.

Next, we will focus on explaining the rationality of the detector proposed in this paper:

1) From the point of view of the decomposition of scattering mechanism: as for the ocean, the most scattering mechanism is surface scattering; as for the target, because of the complex composition, the most scattering mechanism is the combination of the double-bounce scattering, volume scatter and helix scattering by the combination of two or more coherent scatters. Also, we can explain from equation (3) that the helix scattering power $P_h = 2 \cdot Im\{C_{12} + C_{23}\}$ is not present at the ocean surface because of the reflection symmetry of surface scattering, where both C_{12} and C_{23} are zero in $\langle [C] \rangle_s$, while the corresponding in $\langle [C] \rangle_h$ is complex (Zhang et al., 2018). As a result, we can use helix scattering power as a reinforcement factor and do a multiplication operation directly with the sum of the double scattering and volume scattering powers to highlight the target-dominated scattering mechanism and suppress the background.

2) From the perspective of the wave polarization anisotropy: on the one hand, Touzi et al. (Touzi et al., 2004) have demonstrated experimentally that the wave polarization anisotropy can characterize the non-stationarity of the target; the larger the value of ΔS_n , the greater the variation of the signal with transmit-receive polarization. On the other hand, when ships or other man-made objects are irradiated by electromagnetic waves, the variation of the signal with transmit-receive polarization is more significant, due to their complex structures and materials; however, the sea surface is relatively smooth, the change of signal with transmit-receive polarization is smaller. In other words, when ΔS_n characterizes the target, i.e., $\Delta S_n \rightarrow 1$; and when ΔS_n characterizes the sea surface, i.e., $\Delta S_n \rightarrow 0$. Therefore, it is possible to characterize the

difference between the target and the clutter from the perspective of the variation of the signal with the transmit-receive polarization.

3) From the perspective of combining the scattering and anisotropy characteristics: regardless of the scattering mechanism exhibited by the ship, at incidence angles below 60° , the wave polarization anisotropy of the sea surface is usually lower than that of a ship (Touzi et al., 2004), that is, $(\Delta S_n)_{ship} \geq (\Delta S_n)_{sea}$. It should be noted that $0 < \Delta S_n < 1$, so we can consider ΔS_n as a weighting term that tends to 1 when ΔS_n characterizes the target, and tends to 0 when ΔS_n characterizes the clutter. In more detail, when the ΔS_n tends to 1, the $(P_d + P_v) * P_h * \Delta S$ tends to $(P_d + P_v) * P_h$, but when the ΔS_n tends to 0, the $(P_d + P_v) * P_h * \Delta S$ tends to 0. As a result, the combination of the two can effectively highlight the target and suppress clutter.

In summary, the detector proposed in this paper combines the scattering characteristics of the target with wave polarization anisotropy. Through our analysis, we found that even though the target exhibits mainly surface scattering, the combination of two features also can enhance the difference between the target and the sea clutter, helping us distinguish the target from the sea clutter. Moreover, the SCR is also used to evaluate the performance of the detector, and the expression is given by (Gao et al., 2018)

$$SCR_{joint-SA} = 20 \log \frac{joint - SA_T}{joint - SA_C} \quad (9)$$

where the subscripts T and C indicate the target and clutter pixels, respectively.

3.3. GFD

After the new detector was defined, the statistics of the detector need to be characterized to achieve adaptive detection of CFAR in different scenarios. In this paper, the GFD is used to characterize the statistical behavior of joint-SA. The reason for using is that it has been widely used in different fields and has been proven to be an effective method for describing the statistical behavior of sea clutter (Ao et al., 2018; Li et al., 2010). Li et al. (Li et al., 2011) proposed a version of GFD with three parameters and the probability density function (pdf) is given:

$$p(x) = \frac{|\nu| \kappa^\kappa}{\sigma \Gamma(\kappa)} \left(\frac{x}{\sigma} \right)^{\kappa\nu-1}, \sigma, |\nu|, \kappa, x > 0 \quad (10)$$

where ν , κ , σ represent the power, shape, and scale parameters, and $\Gamma(\cdot)$ is the Gamma function.

Although the GFD is an empirical model, it has also been shown to be relatively general (Li et al., 2011). Because the various distributions used to model SAR images can be considered as a special case, including Rayleigh ($\nu=2, \kappa=1$), exponential ($\nu=1, \kappa=2$), Weibull ($\nu=-2$), and so on. So using the parameter estimation method of GFD in (Qin et al., 2012), the detection threshold can be expressed as:

$$m = \begin{cases} \sigma \left(\frac{1}{\kappa} \Gamma^{-1}(1 - P_{fa}) \right)^{\frac{1}{\nu}}, \nu \geq 0 \\ \sigma \left(\frac{1}{\kappa} \Gamma^{-1}(P_{fa}, \kappa) \right)^{\frac{1}{\nu}}, \nu < 0 \end{cases} \quad (11)$$

where $\Gamma(\cdot, \cdot)$ denotes the inverse incomplete Gamma function and P_{fa} is a given value of the false-alarm probability.

4. Experimental Results and Analysis

In this section, experiments were performed on actual full-polarization SAR data sets which include C-band and L-band. Our goal is to certify the correctness of the theoretical analysis

Algorithm 1 Adaptive CFAR Ship Detector Based on joint-SA

Require: The original full-polarization SAR data I ; The temporary image T ; The false alarm ratio $P_{fa}, \nu, \kappa, \sigma, i, j$;

Ensure: The detection result R ;

- 1: Obtain the data size I ;
- 2: $[Row, Col] = size(I)$;
- 3: $T = zeros(Row, Col); R = zeros(Row, Col)$;
- 4: Get the polarimetric covariance matrix $[C]$ and 2×2 scattering matrix $[S]$;
- 5: **for** each pixel $\in I$ **do**
- 6: Carry out the four-component decomposition by using polarimetric covariance matrix $[C]$ and obtain P_d, P_v and P_h ;
- 7: Use the 2×2 scattering matrix $[S]$ getting the extreme of DoP , and then getting the wave polarization anisotropy ΔS , i.e.:
8: $\Delta S = S_n(DoP_{min}) - S_n(DoP_{max})$
- 9: Compute the joint-SA value:
10: $joint - SA = (P_d + P_v) * P_h * \Delta S$
- 11: Add the joint-SA value into T :
12: $T(i, j) = joint - SA$
- 13: **end for**
- 14: Estimate the GFD parameters ν, κ, σ ;
- 15: Set P_{fa} and then compute the threshold m ;
- 16: **if** $\nu \neq 0$ **then**
- 17: $m = \sigma(\frac{1}{\kappa}\Gamma^{-1}(1 - P_{fa}))^{\frac{1}{\nu}}$
- 18: **else**
- 19: $m = \sigma(\frac{1}{\kappa}\Gamma^{-1}(P_{fa}, \kappa))^{\frac{1}{\nu}}$
- 20: **end if**
- 21: **for** each pixel $q \in T$ **do**
- 22: **if** $T(q) > m$ **then**
- 23: Consider q as a ship pixel and then set the corresponding position of q in R to one, i.e.:
24: $R(q) = 1$;
- 25: **else**
26: $R(q) = 0$;
- 27: **end if**
- 28: **end for**
- 29: **return** the detection result R .

in Section 3. First, the fitting abilities of the GFD for different detectors used for CFAR ship detection were accessed. Subsequently, we accessed if the detector based on joint-SA is more effective and can improve the SCR compared with other detectors. Finally, the CFAR detection performance of several detectors was compared.

4.1. Test Data

The experiments are carried out on five SAR data sets, which were collected by using three types of space-borne platforms: the Canada C-band RADARSAT-2, the China C-band GaoFen-3, and the Japan L-band ALOS. Five typical scenes located in the South China Sea, Laizhou Bay, China, the Bohai Sea, China, the Yellow Sea, China, and the Persian Gulf, were selected for the experiments. All data products are fully polarimetric and in the single-look complex (SLC)

format. The Pauli RGB images of scenes 1-5 are shown in Figure 1 (a)-(e), where the color is coded by $|S_{HH} - S_{VV}|_{red}$, $|S_{HH} + S_{VV}|_{blue}$, $2|S_{HV}|_{green}$.

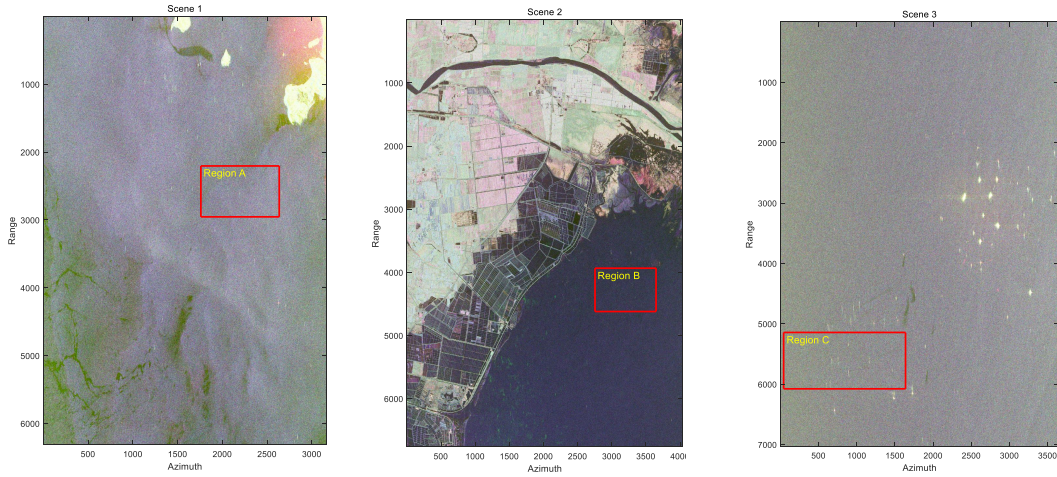
Table 1: Detailed description of the datasets

Scene ID	Product ID	Sensor	Date	Resolution R x A (m)	Incidence Angle(°)	β (°)
1	RD2009000238-0	RADARSAT-2	2009/09/18	8.6 x 4.7	32.35°-34.0°	8.2°
2	PDS_05350120	RADARSAT-2	2016/09/10	6.8 x 5.1	43.61°-44.92°	10.2°
3	PDS_03326690	RADARSAT-2	2011/09/08	7.5 x 4.7	42.77°-44.11°	10.7°
4	2075802	GaoFen-3	2016/11/20	6.4 x 4.1	25.27°-27.80°	2.1°
5	ALPSRP169460500	ALOS	2009/03/30	3.5 x 7.7	21.5°-23.8°	7.8°

When evaluating the performance of different detectors, the ground-truth data is essential. However, for the five data sets in this paper, we don't have ground-truth data, especially Automatic Identification System (AIS) data and meteorological data. Like the methods used in other papers (Zhang et al., 2018, 2020; Gao et al., 2018), we determine the location of ships mainly through visual interpretation methods. This method is effective because the backscattered power from the ship is always stronger than the sea surface and ships appear as a bright spot on the image. In addition, the sea state corresponding to the test data (e.g., the roughness of sea surface) is also necessary for the evaluation of the performance of detectors. Therefore, we use the method in (Hajnsek et al., 2003; Zhang et al., 2019; Yin et al., 2014) to assess the roughness of the sea surface of the test data, with the following equation

$$\text{sinc}(4\beta_1) = \frac{T_{22} - T_{33}}{T_{22} + T_{33}} \quad (12)$$

where $\beta_1 \in [0, 90^\circ]$, the larger the β_1 , the rougher the sea surface, and vice versa.



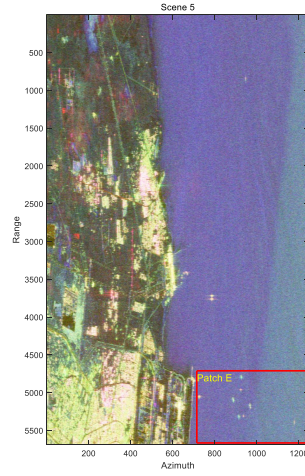
(a) Scene 1

(b) Scene 2

(c) Scene 3



(d) Scene 4



(e) Scene 5

Figure 1: Five experimental scenarios.

4.2. Validation of GFD with Different Detectors

Statistical characterization of detectors is very important for the adaptive detection of detectors, such as the popular CFAR operation in the field of radar signal detection. In this paper, three known excellent detectors, DBSP, RsDVH, ΔS_n were chosen to show and verify the expected effectiveness of the proposed detector joint-SA. The reason for the selection of DBSP, RsDVH and ΔS_n is based on the following facts. On the one hand, the three detectors are excellent for SAR image ship detection. Both ΔS_n , DBSP, and RsDVH have been proven to be effective detectors in characterizing target properties and ocean state and are superior to other detectors in improving the SCR, such as SPAN, PMS, and so on. On the other hand, detector DBSP and RsDVH have a good effect on the detection of relatively weakly scattering targets. Most importantly, it has been proven that the GFD can effectively describe the statistical characterization of the two detectors.

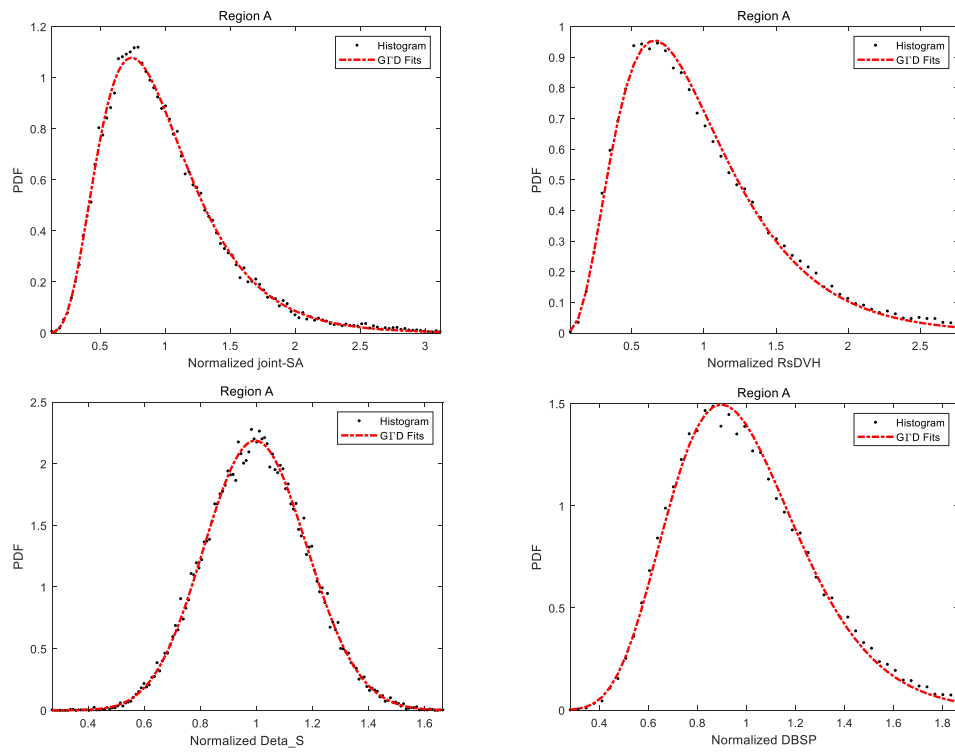


Figure 2: Histograms and the fit results of G1D for different detectors in Region A.

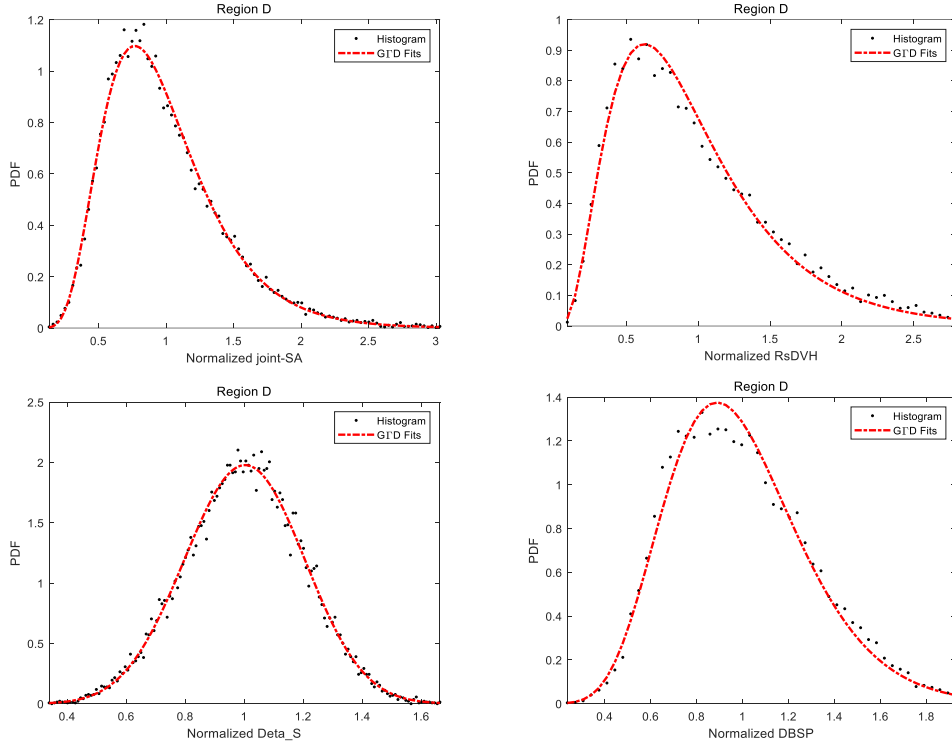


Figure 3: Histograms and the fit results of G1D for different detectors in Region D.

Table 2: Quantitative evaluation of the fitting accuracy of five scenes using KL values for G1D

Detectors	Patch A	Patch B	Patch C	Patch D	Patch E
joint-SA	0.0033	0.0155	0.0057	0.0047	0.0064
RsDVH	0.0041	0.0072	0.0064	0.0086	0.0066
ΔS	0.0068	0.0392	0.0035	0.0136	0.0050
DBSP	0.0037	0.0074	0.0060	0.0075	0.0071

To be fair, in this paper we also choose the G1D to describe the statistical characterization of the proposed detector. The initial intention of doing so is based on the following two considerations: First, compared to other classic statistical models, such as Gaussian, Rayleigh, Gamma, log-normal, Weibull, and K, many results were shown that G1D can obtain higher fitting accuracy for single-channel sea clutter data. Second, G1D is a more advanced and general statistical model, because many statistical models in the field of SAR images are a special case of G1D in theory.

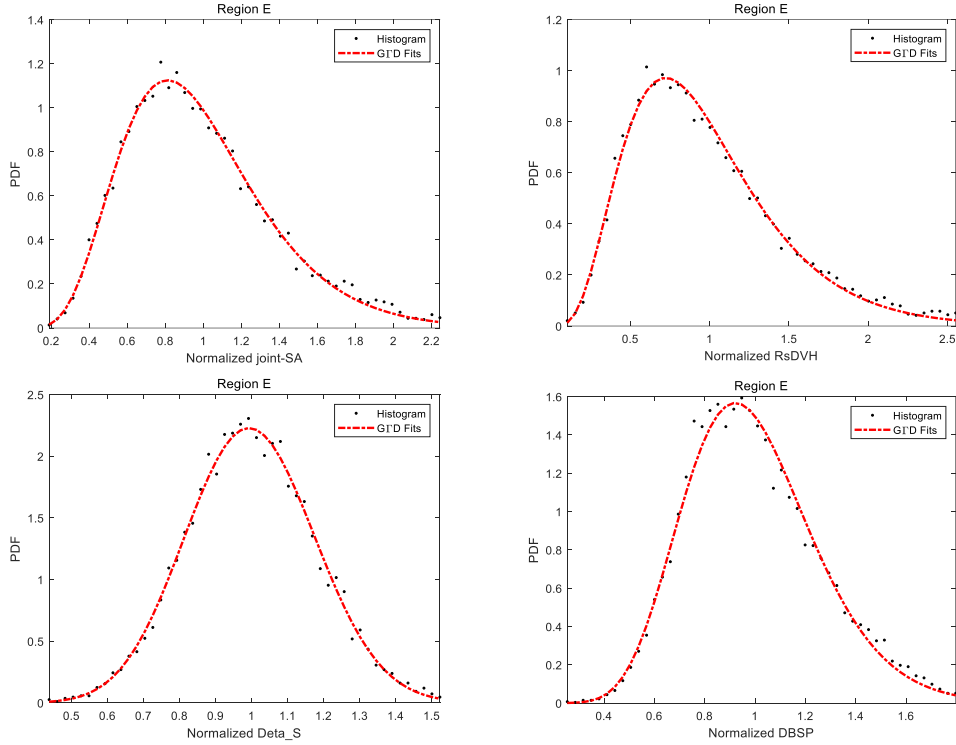


Figure 4: Histograms and the fit results of GFD for different detectors in Region E.

For each region in the scene, we used GFD to fit each of the ΔS_n , DBSP, RsDVH, joint-SA. Meanwhile, to make the fitting results clearer and more intuitive, we normalized all the data before fitting them by dividing them by the mean of the corresponding data. In addition, to better illustrate the fitting accuracy of GFD, the commonly symmetric Kullback-Leibler (KL) (Kullback and Leibler, 1951) distance was introduced, being used as the measure of the difference in similarity between the estimated and theoretical pdfs.

As shown in figures 2, 3, 4 and table 2, the GFD show a good-of-fit for different detectors, and the fitting result could not be affected by external factors, such as radar sensor type, sea surface roughness, etc. Therefore, the results of fitting experiments of the GFD are acceptable, and the GFD can be used as a statistical model for adaptive threshold estimation. Because of the same results and to save space, we only show the fitting results for different satellite platforms and different incidence angles.

4.3. Effectiveness validation of the joint-SA detector

After completing the validation of the GFD for different detectors, we will focus on the effectiveness of the proposed detector for relatively weakly scattering targets. In the next pages, we will compare the ability of different detectors to highlight relatively weakly scattering targets. In the field of SAR image ship detection, the SCR has been regarded as a core physical quantity to evaluate the goodness of a detector. Therefore, we also used the SCR to evaluate detectors mentioned in this paper.

The first thing we must do is select a region that contains relatively weakly scattering targets. A flexible way to process images is to select a chip from scenes that contain only one relatively weakly scattering target and its local background. The initial intention of doing this is based on two considerations. On the one hand, from the perspective of target highlighting, the region containing only one target can show the state of the target and the background more intuitively and ensure that the target is not affected by other factors. On the other hand, from the visual point of view, it is possible to explore and reveal the details of different detectors more clearly in a limited space. It should be noted that due to the lack of AIS data, all ships in the paper were visually gained from images by trained image interpreters.

First, we performed qualitative analysis and quantitative evaluation on the relatively weakly scattering target from region A in scene 1, which is related to C-band RADARSAT-2 and the incidence angle of scene 1 is $[32.35^\circ, 34.01^\circ]$. As figure 5 showed, (a) is the Pauli image with a relatively weakly scattering target, and (b), (c), (e), (f) is the 3-D image with different detectors. As can we see, joint-SA performs best in target highlighting and clutter suppression, while RsDVH, ΔS , and DBSP are unable to distinguish the target. To further illustrate the effectiveness of joint-SA, we compared the SCR values of the four detectors, as shown in figure 5 (d). The detector joint-SA has the highest SCR value of 33.17 (dB), which is twice as high as the detector RsDVH, 10 times as high as ΔS , and 4 times as high as DBSP. Therefore, from both qualitative analysis and quantitative evaluation, we can conclude that joint-SA is better than the other detectors in this group of experiments.

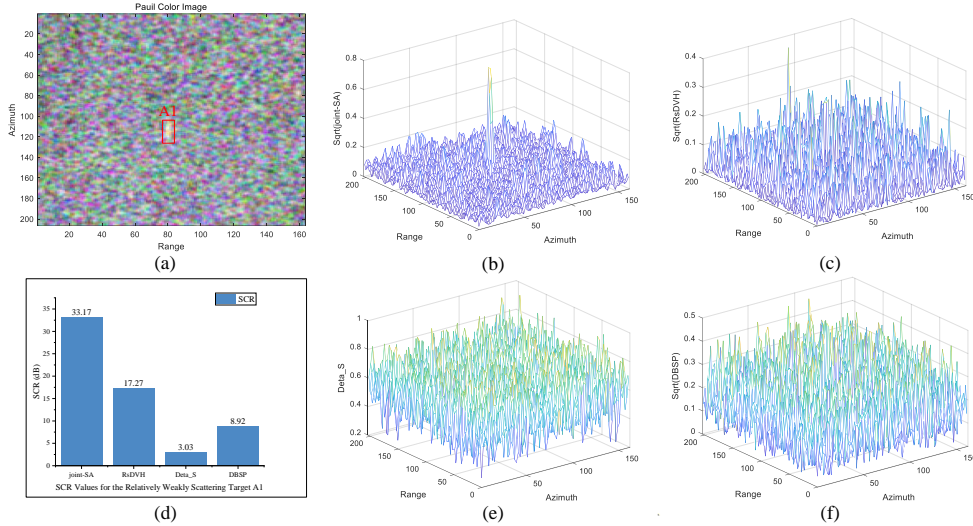


Figure 5: Comparison of different detectors of a relatively weakly scattering ship on region A in scene 1. (a) Pauli RGB image. (b) 3-D display of the joint-SA for the interval $[0,1]$. (c) 3-D display of the RsDVH for the interval $[0,1]$. (d) SCR value for the target A1. (e) 3-D display of the ΔS for the interval $[0,1]$. (f) 3-D display of the DBSP for the interval $[0,1]$.

Second, we performed qualitative analysis and quantitative evaluation on the target from region D in scene 4, which is related to C-band GF-3, and the incidence angle of scene 4 is $[25.27^\circ, 27.80^\circ]$. As shown in figure 6, like the first set of experiments, the detector joint-SA outperforms the other three detectors. As can be seen in figure 6 (b), joint-SA has a very good ability to suppress the clutter and highlight the target. In addition, the SCR value of the detector joint-SA is higher than this of the other three detectors, as can be seen in figure 6 (d). This

is consistent with the 3-D visualization results plot. Hence, the detector joint-SA is also better than the other detectors in this set of experiments.

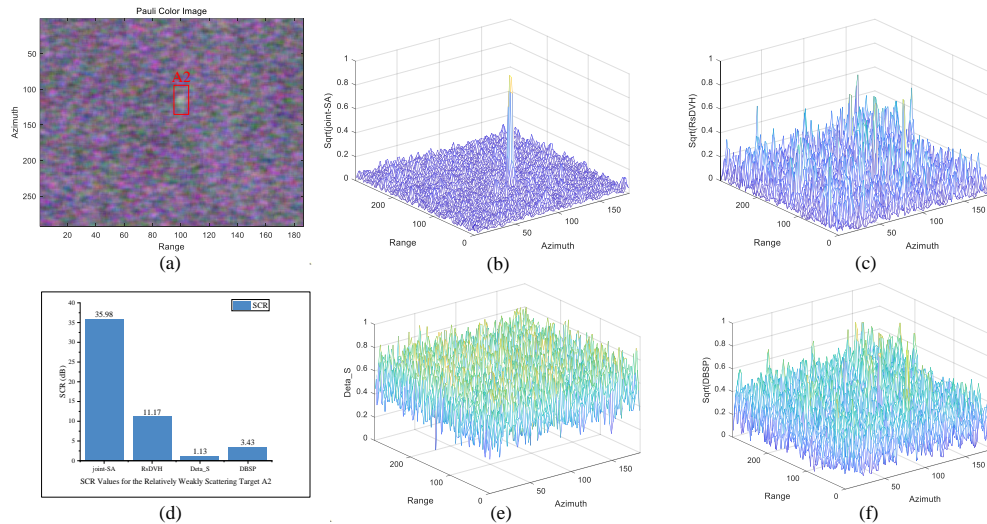


Figure 6: Comparison of different detectors of a relatively weakly scattering ship on region D in scene 4. (a) Pauli RGB image. (b) 3-D display of the joint-SA for the interval $[0,1]$. (c) 3-D display of the RsDVH for the interval $[0,1]$. (d) SCR value for the target A2. (e) 3-D display of the ΔS for the interval $[0,1]$. (f) 3-D display of the DBSP for the interval $[0,1]$.

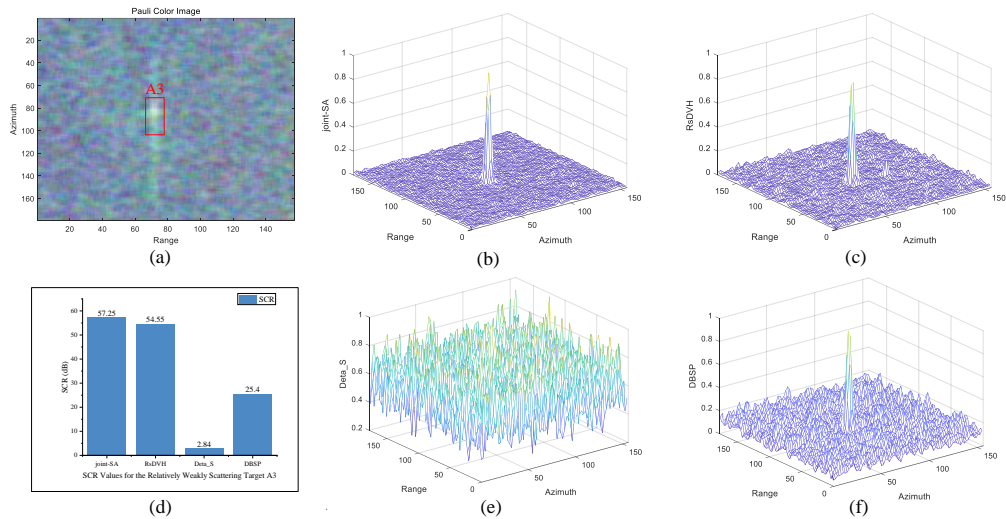


Figure 7: Comparison of different detectors of a relatively weakly scattering ship on region E in scene 5. (a) Pauli RGB image. (b) 3-D display of the joint-SA for the interval $[0,1]$. (c) 3-D display of the RsDVH for the interval $[0,1]$. (d) SCR value for the target A3. (e) 3-D display of the ΔS for the interval $[0,1]$. (f) 3-D display of the DBSP for the interval $[0,1]$.

Third, we performed qualitative analysis and quantitative evaluation on the target from region

E in scene 5, which is related to L-band ALOS. The incidence angle of scene 5 is $[21.5^\circ, 23.8^\circ]$. As shown in figure 7, except for the detector ΔS , all three detectors can easily distinguish the targets, and the peaks of the three detectors are similar. But for the DBSP, the clutter rejection is worse than that of joint-SA and RsDVH. To compare the ability of these three detectors to highlight the target, we also compare their SCR values, as shown in figure 7 (d), the SCR value of the three detectors is 57.25 dB, 54.55 dB, and 25.40 dB, which are consistent with the performance in the 3-D images. Therefore, the detector joint-SA is also better than the other detectors in this set of experiments.

Because of the same results, region B in scene 2 and region C in scene 3 which is related to the RADARSAT-2 in C-band type, we do not analyze in detail. Through the above three sets of experiments, we can conclude that the four detectors have different sensitivities to clutter pixels and target pixels in different regions, and the proposed ship detector joint-SA is better than any of the detectors compared in this paper, both in terms of target prominence, clutter rejection, and SCR values. In addition, we can also see that in the scenes with low incidence angles, detectors joint-SA, RsDVH and DBSP have good performance results, but with the increasing incidence angles, the effectiveness of detectors RsDVH and DBSP is decreasing, while for the joint-SA, the effectiveness does not change with the incidence angle when the incidence angle is less than 45° .

4.4. Comparison of CFAR results with different detectors

In section 4.2, we have verified the GFD can be used to describe the statistics of the four detectors, which provides the possibility to subsequently compare the CFAR detection performance of the four detectors. In section 4.3, we also demonstrated that the detector joint-SA outperforms ΔS , DBSP, and RsDVH in SCR. Therefore, we can conclude that the proposed detector in this paper still outperforms the other three detectors in CFAR adaptive detection. Next, we will prove our point with experiments. It should be noted that the p_{fa} is 10^{-5} in this paper.

The first experiment will use region A in scene 1. The incidence angle of scene 1 is $[32.35^\circ, 34.01^\circ]$. As can be seen in figure 8 (a), there are seven weakly scattering ships. The detector joint-SA detected five targets without false alarms. While for the RsDVH and DBSP, they detected only two targets, but with three false alarms. Therefore, from the perspective of detection accuracy, joint-SA is superior to the other three detectors. As shown in figure 11, the average SCR value of joint-SA is also higher than the other three detectors. To further analyze the detection performance of the four detectors, we counted the SCR values of them. As can be seen in table 3, the SCR values of joint-SA of T3 and T5 are 12.92 dB and 13.03 dB, respectively, which are the lowest among all targets. For both RsDVH and DBSP, the undetected targets are those with low SCR values, and surprisingly, the SCR value of target T2 appears negative in both detectors. Therefore, joint-SA is superior to the other four detectors in terms of detection accuracy and SCR.

Table 3: The SCR values for relatively weakly scattering targets in region A

Detectors	T1	T2	T3	T4	T5	T6	T7
RsDVH	25.95	-0.67	4.75	22.59	10.01	26.28	21.08
ΔS	0.69	-0.35	2.53	2.46	1.80	1.70	2.32
DBSP	20.97	-0.47	2.72	20.12	9.99	26.71	21.64
joint-SA	38.65	13.88	12.92	24.41	13.03	42.15	46.66

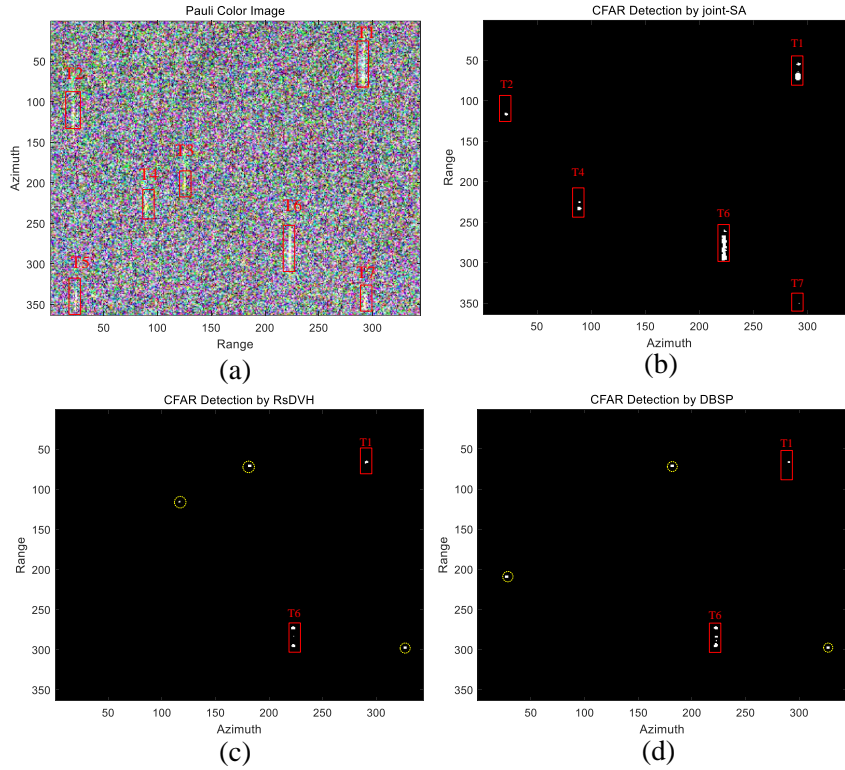


Figure 8: Detection results of region A in scene 1. (a) Pauli RGB image. (b) CFAR detection result by joint-SA. (c) CFAR detection result by RsDVH. (d) CFAR detection result by DBSP. Yellow dashed circles: false-alarm targets, and the red boxes: targets

The second set of experiments will be conducted on region B scene 2 which is related to the C-band RADARSAT-2. The incidence angle of scene 2 is $[43.61^\circ, 44.92^\circ]$. As can be seen from figure 9, there are 8 relatively weakly scattering targets in this scene. In terms of the detection accuracy, joint-SA successfully detected all targets, while RsDVH and DBSP detected 6, and 4 targets, respectively. To further evaluate the performance of the four detectors, we also counted the average SCR values of the eight targets. It can also be seen from figure 11 that the average SCR value for the 8 targets, joint-SA is the highest among all detectors. In table 4, targets T4 and T5 were missed with SCR values of 9.21 dB and 8.97 dB in RsDVH, respectively, with the lowest SCR values among RsDVH, and the difference in SCR value between T5 (8.97 dB) and T1 (40.44 dB) is about 5 times. A similar situation occurred in the DBSP, where targets with lower SCR values were not detected, and the difference between T4 (3.37 dB) and T1 (17.01 dB) is 5 times. It is the large difference in SCR values that leads to incorrect estimation in CFAR adaptive threshold estimation and thus targets miss.

Table 4: The SCR values for relatively weakly scattering targets in region B

Detectors	T1	T2	T3	T4	T5	T6	T7	T8
RsDVH	40.44	25.42	22.43	9.21	8.97	24.02	23.94	24.78
ΔS	0.76	1.47	1.82	0.41	0.44	-0.04	1.32	-0.48
DBSP	17.01	11.1	8.01	3.37	4.05	9.49	12.79	9.63
joint-SA	48.77	27.95	28.22	40.68	17.84	25.56	26.03	27.11

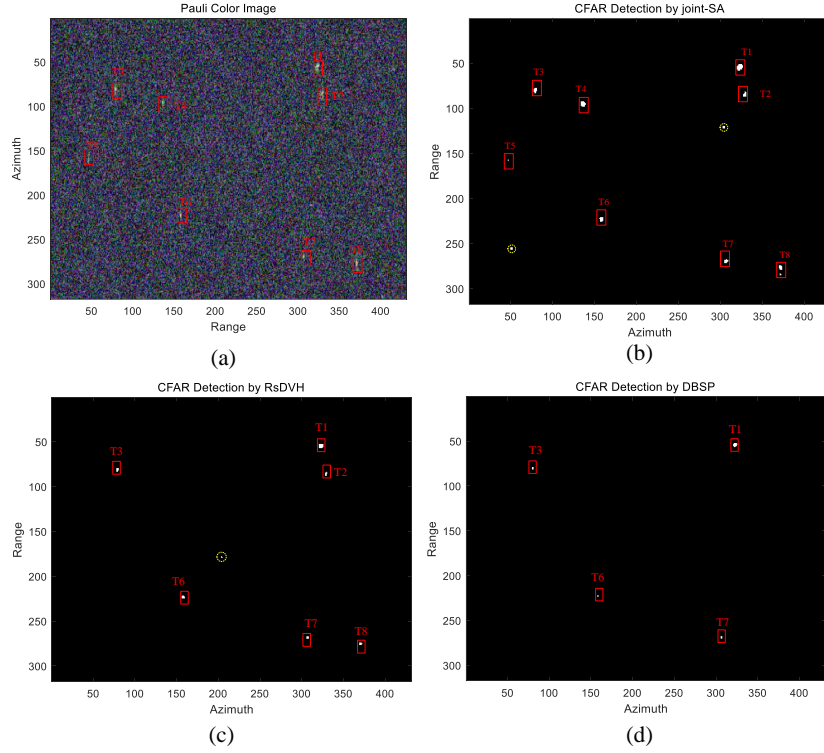


Figure 9: Detection results of region B in scene 2. (a) Pauli RGB image. (b) CFAR detection result by joint-SA. (c) CFAR detection result by RsDVH. (d) CFAR detection result by DBSP. Yellow dashed circles: false-alarm targets, and the red boxes: targets.

The third experiment will use region D in scene 4. The incidence angle is $[25.27^\circ, 27.80^\circ]$. As can be seen in figure 10 (a), there are six relatively weakly scattering targets in this region. From the (b), (c), (d), we can see that the detector joint-SA successfully detected 6 targets, while detectors RsDVH and DBSP only detected 4 targets. In terms of detection accuracy, joint-SA is better than RsDVH and DBSP. It can also be seen from figure 11 that the average SCR value of joint-SA is much larger than those of RsDVH and DBSP. Therefore, both in terms of detection accuracy and SCR values, joint-SA is better than the other detectors.

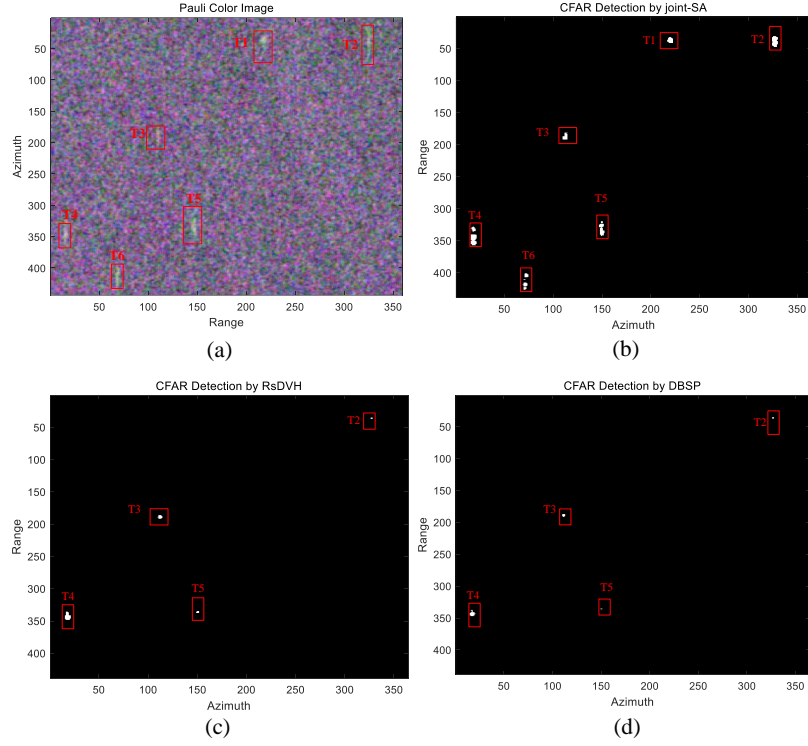


Figure 10: Detection results of region D in scene 4. (a) Pauli RGB image. (b) CFAR detection result by joint-SA. (c) CFAR detection result by RsDVH. (d) CFAR detection result by DBSP. Yellow dashed circles: false-alarm targets, and the red boxes: targets.

Table 5: The SCR values for relatively weakly scattering targets in region D

Detectors	T1	T2	T3	T4	T5	T6
RsDVH	14.09	26.67	28.97	42.46	18.99	4.91
ΔS	2.48	1.43	1.86	1.35	1.15	0.86
DBSP	4.74	14.18	9.93	17.79	6.53	2.94
joint-SA	37.67	55.73	33.38	54.87	37.81	33.92

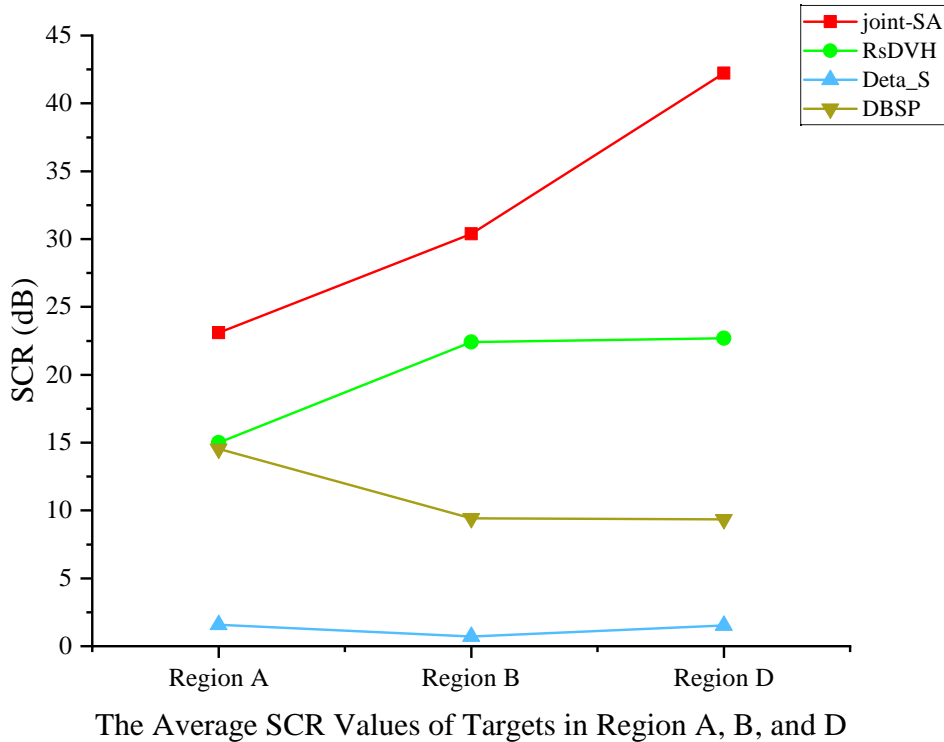


Figure 11: The average SCR values of targets in regions A, B, and D.

Similarly, we counted the SCR of six relatively weakly scattering targets in different detectors. As can be seen in table 5, the joint-SA has higher SCR values than the other four detectors. For the detectors joint-SA, the difference in SCR values for individual targets is small, while the difference in SCR values for individual targets in RsDVH and DBSP is large. We can see that the SCR values of T1 and T6 are 14.09 dB and 4.91 dB, respectively, which are the smallest SCR values among all targets, and the largest SCR value T4 is 42.46, which is 9 times different from the smallest T6. It is the huge difference in SCR values between different targets that leads to the inability to estimate the threshold correctly in the CFAR adaptive detection stage, thus making T1 and T6 missed detections, and the same reason for the detector DBSP.

In our experiments, we found that some targets with low average SCR values were detected, while some targets with high average SCR values were not detected. This phenomenon is reasonable for the following reasons: on the one hand, it should be noted that since we can't know all pixels of targets accurately, we calculate the SCR value by boxing the target and the clutter region, average the values in the region, and then calculating the SCR. Therefore, a high average SCR does not mean that every target pixel has a high SCR value, but vice versa. On the other hand, when a target with a low average SCR value has a pixel with a high SCR value, the target will also be detected, and conversely, when the target has high average SCR values, but every single pixel is slightly lower, the target will not be detected.

To save space, we don't analyze for region B in scene 2 and region E in scene 5 in detail and only show their detection result, as figures 12, 13, and tables 6, 7. Noted ΔS that cannot

effectively perform adaptive ship detection in these 5 scenes, so we do not analyze it. In summary, the proposed detector joint-SA is better than the other ship detectors (DBSP, RsDVH, ΔS , and so on) in terms of both the accuracy of ship detection and the SCR value, and more importantly, the detection performance of joint-SA does not vary with the incidence angles.

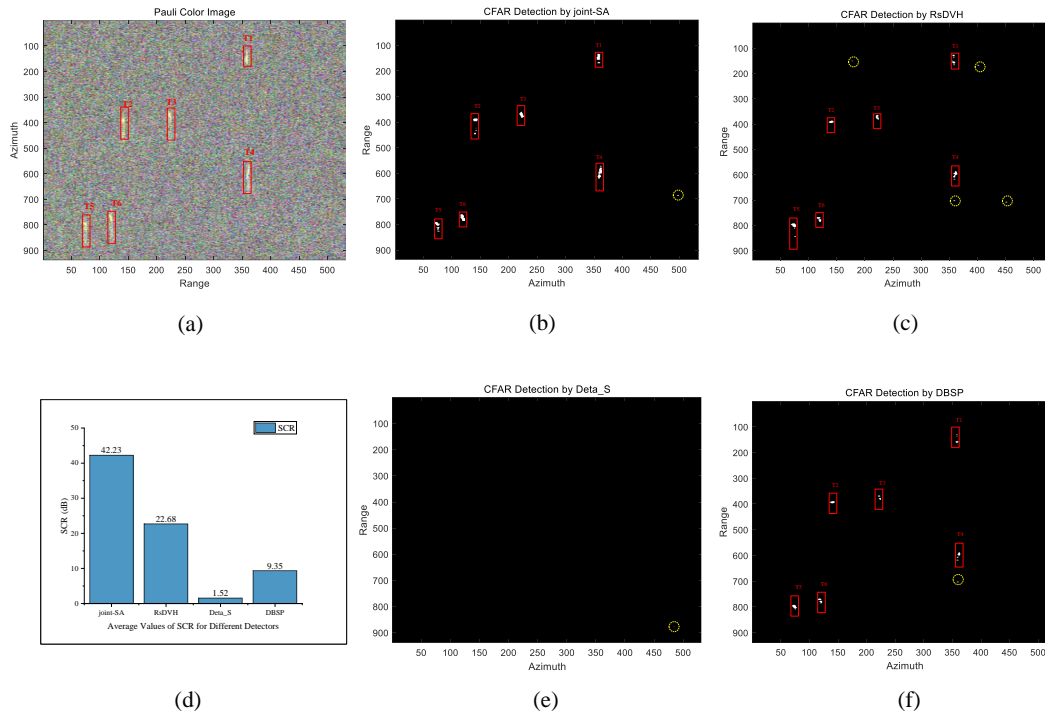


Figure 12: Detection results of region C in scene 3. (a) Pauli RGB image. (b) CFAR detection result by joint-SA. (c) CFAR detection result by RsDVH. (d) Average values of SCR for different detectors. (e) CFAR detection result by ΔS . (f) CFAR detection result by DBSP. Yellow dashed circles: false-alarm targets, and the red boxes: targets.

Table 6: The SCR values for relatively weakly scattering targets in region C

Detectors	T1	T2	T3	T4	T5	T6
RsDVH	35.44	54.28	36.18	39.25	54.88	42.37
ΔS	0.95	0.98	0.81	1.25	1.45	1.38
DBSP	14.43	24.78	15.02	15.99	24.88	19.82
joint-SA	36.42	62.55	44.82	50.54	61.70	50.19

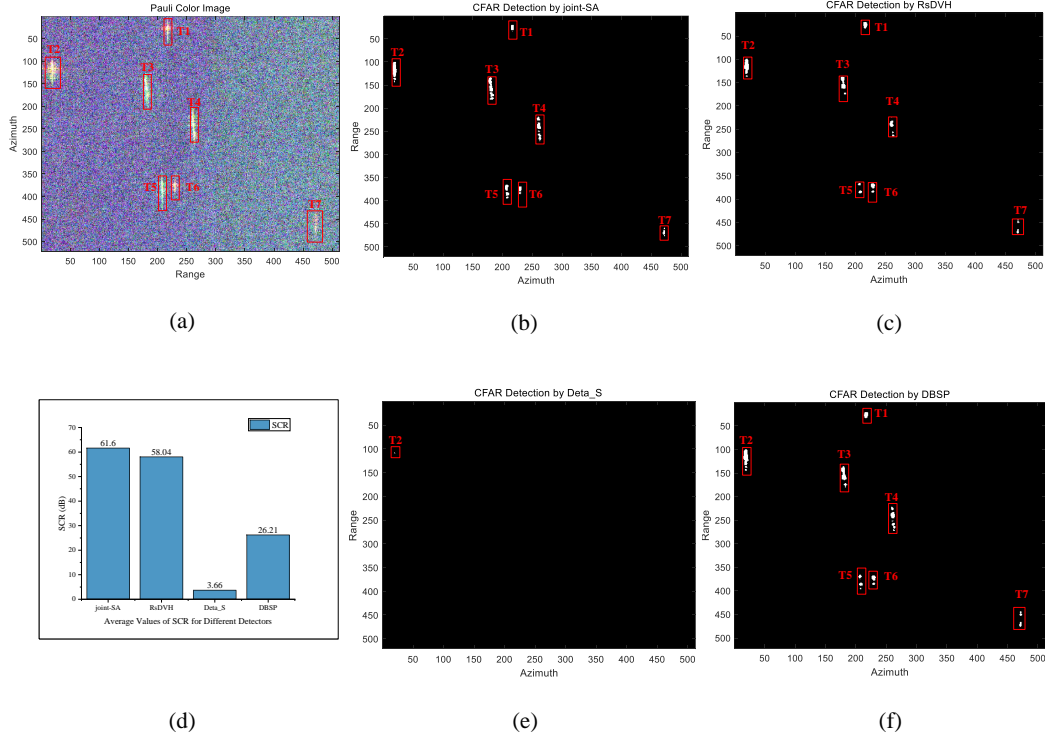


Figure 13: Detection results of region E in scene 5. (a) Pauli RGB image. (b) CFAR detection result by joint-SA. (c) CFAR detection result by RsDVH. (d) Average values of SCR for different detectors. (e) CFAR detection result by ΔS . (f) CFAR detection result by DBSP. Yellow dashed circles: false-alarm targets, and the red boxes: targets.

Table 7: The SCR values for relatively weakly scattering targets in region E

Detectors	T1	T2	T3	T4	T5	T6	T7
RsDVH	57.92	84.79	52.95	50.08	47.52	62.64	28.48
ΔS	4.23	2.02	3.54	4.04	4.28	4.54	3.01
DBSP	26.99	37.59	26.29	24.58	22.09	28.27	17.67
joint-SA	64.26	73.79	62.82	72.65	59.24	65.31	33.16

5. Conclusion and Discussion

To realize the detection of relatively weakly scattering targets and improve the detection accuracy, we proposed a new full-polarization SAR image ship detector joint-SA, by joint the target scattering characteristics and the wave polarization anisotropy. First, we tested and verified the suitability of the GFD for characterizing joint-SA statistics of sea clutter with a wide range of homogeneity. Second, from the perspective of the SCR, we strictly demonstrated that the detector is an effective physical quantity to distinguish the ship from the sea clutter. Third, using the GF-3 in C-band type, the RADARSAT-2 in C-band type data, and the L-band ALOS

data, we verified the correctness of the theory of the detector joint-SA and the superiority of the detection accuracy.

Because joint-SA considers two different characteristics: scattering characteristics and wave polarization anisotropy, the detector joint-SA can effectively improve SCR values and the accuracy of ship detection. Experiments were conducted using SAR data from different satellite platforms, wavebands, and incidence angles, and the experimental results proved that the performance of the detector joint-SA is better than the other three detectors when the incidence angles are less than 45° , and its performance does not vary with the incidence angle. That is to say, the robustness of joint-SA is better than the other three detectors. As a result, we can conclude that detector joint-SA is a flexible full-polarization ship detector that outperforms the other three detectors.

Since we lack data for incidence angles higher than 45° , we cannot verify the validity of joint-SA on high incidence angle SAR data. In future work, we should deal with these defects with other efficient characteristics. As for the detection performance in high sea state and incidence angles, we will continue to validate it when more PolSAR data and AIS data are available.

Acknowledgments

This work was supported in part by the National Natural Science Foundation of China under Project 41822105, in part by Key Research Plan of Hunan Province under Project 2019SK2173, and in part by the Fundamental Research Funds for the Central Universities under Projects 2682020ZT34 and 2682021CX071.

References

- AN, W., ZHANG, W., YANG, J., HONG, W., CAO, F., 2009. On the similarity parameter between two targets for the case of multi-look polarimetric sar. *Chinese journal of electronics* 18, 545–550.
- Ao, W., Xu, F., Li, Y., Wang, H., 2018. Detection and discrimination of ship targets in complex background from spaceborne alos-2 sar images. *IEEE Journal of Selected Topics in Applied Earth Observations and Remote Sensing* 11, 536–550.
- Bicout, D., Brosseau, C., 1992. Multiply scattered waves through a spatially random medium: entropy production and depolarization. *Journal de Physique I* 2, 2047–2063.
- Chaney, R., Bud, M., Novak, L., 1990. On the performance of polarimetric target detection algorithms. *IEEE Aerospace and Electronic Systems Magazine* 5, 10–15.
- Chini, M., Hostache, R., Giustarini, L., Matgen, P., 2017. A hierarchical split-based approach for parametric thresholding of sar images: Flood inundation as a test case. *IEEE Transactions on Geoscience and Remote Sensing* 55, 6975–6988.
- Ciuonzo, D., Carotenuto, V., De Maio, A., 2017. On multiple covariance equality testing with application to sar change detection. *IEEE Transactions on Signal Processing* 65, 5078–5091.
- Cloude, S.R., Pottier, E., 1996. A review of target decomposition theorems in radar polarimetry. *IEEE transactions on geoscience and remote sensing* 34, 498–518.
- Deschamps, G., Mast, P., 1973. Poincaré sphere representation of partially polarized fields. *IEEE Transactions on Antennas and Propagation* 21, 474–478.

- Ferrara, G., Migliaccio, M., Nunziata, F., Sorrentino, A., 2011. Generalized-k (gk)-based observation of metallic objects at sea in full-resolution synthetic aperture radar (sar) data: A multipolarization study. *IEEE Journal of Oceanic Engineering* 36, 195–204.
- Freeman, A., Durden, S.L., 1998. A three-component scattering model for polarimetric sar data. *IEEE transactions on geoscience and remote sensing* 36, 963–973.
- Gao, G., Gao, S., He, J., Li, G., 2018. Adaptive ship detection in hybrid-polarimetric sar images based on the power–entropy decomposition. *IEEE Transactions on Geoscience and Remote Sensing* 56, 5394–5407.
- Gao, G., Shi, G., Zhou, S., 2013. Ship detection in high-resolution dual-polarization sar amplitude images. *International Journal of Antennas and Propagation* 2013.
- Guissard, A., 1994. Mueller and kennaugh matrices in radar polarimetry. *IEEE Transactions on geoscience and remote sensing* 32, 590–597.
- Guo, R., Zhang, L., Li, J., Xing, M., Zang, B., Bao, Z., 2011. A novel strategy of nonnegative-matrix-factorization-based polarimetric ship detection. *IEEE Geoscience and Remote Sensing Letters* 8, 1085–1089.
- Hajnsek, I., Pottier, E., Cloude, S.R., 2003. Inversion of surface parameters from polarimetric sar. *IEEE Transactions on Geoscience and Remote Sensing* 41, 727–744.
- Jakeman, E., Tough, R., 1987. Generalized k distribution: a statistical model for weak scattering. *JOSA A* 4, 1764–1772.
- Kostinski, A.B., James, B.D., Boerner, W.M., 1988. Optimal reception of partially polarized waves. *JOSA A* 5, 58–64.
- Kullback, S., Leibler, R.A., 1951. On information and sufficiency. *The annals of mathematical statistics* 22, 79–86.
- Lee, J.S., Pottier, E., 2017. *Polarimetric radar imaging: from basics to applications*. CRC press.
- Li, H.C., Hong, W., Wu, Y.R., Fan, P.Z., 2010. An efficient and flexible statistical model based on generalized gamma distribution for amplitude sar images. *IEEE Transactions on Geoscience and Remote Sensing* 48, 2711–2722.
- Li, H.C., Hong, W., Wu, Y.R., Fan, P.Z., 2011. On the empirical-statistical modeling of sar images with generalized gamma distribution. *IEEE Journal of selected topics in signal processing* 5, 386–397.
- Liao, M., Wang, C., Wang, Y., Jiang, L., 2008. Using sar images to detect ships from sea clutter. *IEEE Geoscience and Remote Sensing Letters* 5, 194–198.
- Liu, T., Zhang, J., Gao, G., Yang, J., Marino, A., 2019. Cfar ship detection in polarimetric synthetic aperture radar images based on whitening filter. *IEEE Transactions on Geoscience and Remote Sensing* 58, 58–81.
- Marino, A., 2013. A notch filter for ship detection with polarimetric sar data. *IEEE Journal of Selected Topics in Applied Earth Observations and Remote Sensing* 6, 1219–1232.
- Marino, A., Cloude, S.R., Woodhouse, I.H., 2012. Detecting depolarized targets using a new geometrical perturbation filter. *IEEE Transactions on Geoscience and Remote Sensing* 50, 3787–3799.

- Martín-de Nicolás, J., Jarabo-Amores, M.P., Mata-Moya, D., del Rey-Maestre, N., Bárcena-Humanes, J.L., 2014. Statistical analysis of sar sea clutter for classification purposes. *Remote Sensing* 6, 9379–9411.
- Ohki, M., Shimada, M., 2018. Large-area land use and land cover classification with quad, compact, and dual polarization sar data by palsar-2. *IEEE Transactions on Geoscience and Remote Sensing* 56, 5550–5557.
- Principe, J.C., Radisavljevic, A., Fisher, J., Hiett, M., Novak, L.M., 1998. Target prescreening based on a quadratic gamma discriminator. *IEEE Transactions on Aerospace and Electronic Systems* 34, 706–715.
- Qin, X., Zhou, S., Zou, H., Gao, G., 2012. A cfar detection algorithm for generalized gamma distributed background in high-resolution sar images. *IEEE Geoscience and Remote Sensing Letters* 10, 806–810.
- Renga, A., Graziano, M.D., Moccia, A., 2018. Segmentation of marine sar images by sublook analysis and application to sea traffic monitoring. *IEEE Transactions on Geoscience and Remote Sensing* 57, 1463–1477.
- Robey, F.C., Fuhrmann, D.R., Kelly, E.J., Nitzberg, R., 1992. A cfar adaptive matched filter detector. *IEEE Transactions on aerospace and electronic systems* 28, 208–216.
- Schleher, D., 1976. Radar detection in weibull clutter. *IEEE Transactions on Aerospace and Electronic Systems* , 736–743.
- Shirvany, R., Chabert, M., Tourneret, J.Y., 2012. Ship and oil-spill detection using the degree of polarization in linear and hybrid/compact dual-pol sar. *IEEE Journal of Selected Topics in Applied Earth Observations and Remote Sensing* 5, 885–892.
- Snapir, B., Waive, T.W., Biermann, L., 2019. Maritime vessel classification to monitor fisheries with sar: Demonstration in the north sea. *Remote Sensing* 11, 353.
- Tian, S., Wang, C., Zhang, H., 2015. Ship detection method for single-polarization synthetic aperture radar imagery based on target enhancement and nonparametric clutter estimation. *Journal of Applied Remote Sensing* 9, 096073.
- Touzi, R., 2000. Calibrated polarimetric sar data for ship detection, in: *IGARSS 2000. IEEE 2000 International Geoscience and Remote Sensing Symposium. Taking the Pulse of the Planet: The Role of Remote Sensing in Managing the Environment. Proceedings (Cat. No. 00CH37120)*, IEEE. pp. 144–146.
- Touzi, R., Charbonneau, F., Hawkins, R., Vachon, P., 2004. Ship detection and characterization using polarimetric sar. *Canadian Journal of Remote Sensing* 30, 552–559.
- Touzi, R., Goze, S., Le Toan, T., Lopes, A., Mougin, E., 1992. Polarimetric discriminators for sar images. *IEEE Transactions on Geoscience and Remote Sensing* 30, 973–980.
- Velotto, D., Soccorsi, M., Lehner, S., 2013. Azimuth ambiguities removal for ship detection using full polarimetric x-band sar data. *IEEE transactions on geoscience and remote sensing* 52, 76–88.
- Wackerman, C.C., Friedman, K.S., Pichel, W.G., Clemente-Colón, P., Li, X., 2001. Automatic detection of ships in radarsat-1 sar imagery. *Canadian journal of remote sensing* 27, 568–577.

- Yamaguchi, Y., Moriyama, T., Ishido, M., Yamada, H., 2005. Four-component scattering model for polarimetric sar image decomposition. *IEEE Transactions on Geoscience and Remote Sensing* 43, 1699–1706.
- Yang, H., Cao, Z., Cui, Z., Pi, Y., 2019. Saliency detection of targets in polarimetric sar images based on globally weighted perturbation filters. *ISPRS Journal of Photogrammetry and Remote Sensing* 147, 65–79.
- Yang, J., Peng, Y.N., Lin, S.M., 2001. Similarity between two scattering matrices. *Electronics Letters* 37, 193–194.
- Yeremy, M., Campbell, J., Mattar, K., Potter, T., 2001. Ocean surveillance with polarimetric sar. *Canadian Journal of Remote Sensing* 27, 328–344.
- Yin, J., Yang, J., Zhou, Z.S., Song, J., 2014. The extended bragg scattering model-based method for ship and oil-spill observation using compact polarimetric sar. *IEEE Journal of Selected Topics in Applied Earth Observations and Remote Sensing* 8, 3760–3772.
- Zhang, C., Zhang, H., Wang, C., Fu, Q., Xu, L., 2017. A novel ship detection method based on shannon entropy in chinese gaofen-3 fully polarimetric sar images, in: *2017 Progress in Electromagnetics Research Symposium-Fall (PIERS-FALL)*, IEEE. pp. 909–916.
- Zhang, T., Ji, J., Li, X., Yu, W., Xiong, H., 2018. Ship detection from polsar imagery using the complete polarimetric covariance difference matrix. *IEEE Transactions on Geoscience and Remote Sensing* 57, 2824–2839.
- Zhang, T., Jiang, L., Xiang, D., Ban, Y., Pei, L., Xiong, H., 2019. Ship detection from polsar imagery using the ambiguity removal polarimetric notch filter. *ISPRS Journal of Photogrammetry and Remote Sensing* 157, 41–58.
- Zhang, T., Yang, Z., Gan, H., Xiang, D., Zhu, S., Yang, J., 2020. Polsar ship detection using the joint polarimetric information. *IEEE Transactions on Geoscience and Remote Sensing* 58, 8225–8241.